Development and characterization of a purified pyrophyllite-based ultrafiltration membrane for the treatment of dye-contaminated water

Development and characterization of a purified pyrophyllite-based ultrafiltration membrane for the treatment of dye-contaminated water

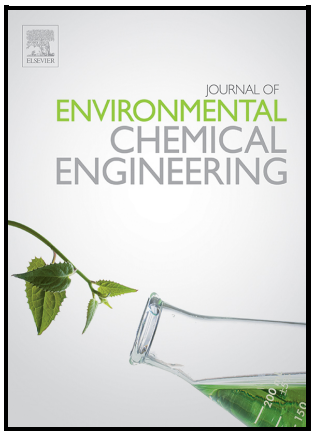

S. Adlane, A. Essate, J. Naim, B. Achiou, A. Tiraferri, A. Aaddane, S. Youssefi, M. Ouammou, S. Alami Younssi

PII: S2213-3437(25)03275-0

DOI: https://doi.org/10.1016/j.jece.2025.118579

Reference: JECE118579

To appear in: *Journal of Environmental Chemical Engineering*

Received date: 22 May 2025
Revised date: 31 July 2025
Accepted date: 8 August 2025

Please cite this article as: S. Adlane, A. Essate, J. Naim, B. Achiou, A. Tiraferri, A. Aaddane, S. Youssefi, M. Ouammou and S. Alami Younssi, Development and characterization of a purified pyrophyllite-based ultrafiltration membrane for the treatment of dye-contaminated water, *Journal of Environmental Chemical Engineering,* (2025) doi:https://doi.org/10.1016/j.jece.2025.118579

Development and characterization of a purified pyrophyllite-based ultrafiltration membrane for the treatment of dye-contaminated water

S. Adlane[1, *], A. Essate[1], J. Naim[1], B. Achiou[1, 2, *], A. Tiraferri[3], A. Aaddane[1], S. Youssefi[1], M. Ouammou[1], S. Alami Younssi[1]

[1]Laboratory of Materials, Membranes and Environment, Faculty of Sciences and Technologies of Mohammedia, Hassan II University of Casablanca, Morocco

[2]Institute of Science, Technology & Innovation (IST&I), Mohammed VI Polytechnic University (UM6P), Ben Guerir, 43150, Morocco

[3]Department of Environment, Land and Infrastructure Engineering, Politecnico di Torino, Corso Duca degli Abruzzi 24, 10129 Turin, Italy

*Corresponding authors: sanaa.adlane-etu@etu.univh2c.ma (S. Adlane); brahim.achiou@fstm.ac.ma (B. Achiou)

Abstract

This study reports the development and optimization of a low-cost ultrafiltration (UF) membrane fabricated from purified pyrophyllite clay for the removal of organic dyes from wastewater. The raw clay, sourced from Morocco, underwent sequential sedimentation, carbonate removal, and organic matter elimination. The purification reduced average particle size from 11.70 to 1.14 μm and minimized loss on ignition from 4.25 to 0.07 wt%. The optimized membrane produced following clay purification, was sintered at temperatures between 1000 and 1100 °C. Among these conditions, SC1050 membrane (sedimentation and carbonate removal, sintered at 1050 °C) exhibited the best trade-off between permeability and selectivity. It achieved a water permeability of 86 L m^{-2} h^{-1} bar^{-1} and a direct red 80 dye rejection of 91.4%. The membrane also rejected 92.9% of methylene blue (cationic) and 81.4% of Congo red (anionic), indicating performance governed mainly by electrostatic interactions. Fouling tests showed a flux recovery ratio of 89.9% and a low irreversible fouling ratio of

10.1%. Cost analysis estimated the total membrane production cost at USD 14.3 m^{-2}, substantially lower than commercial ceramic membranes (USD 500–1000 m^{-2}). These findings indicate that purified pyrophyllite is a promising geomaterial for cost-effective and high-performance UF membranes, offering a potentially scalable and sustainable solution for textile wastewater treatment.

Keywords: Pyrophyllite; Geomaterials; Purification; Ceramic membrane; Ultrafiltration; Fouling; Dyes.

1. Introduction

The rapid growth of the global population has driven the expansion of the textile industry, leading to the generation of large volumes of textile wastewater. This wastewater poses a serious environmental threat as it often contains toxic, mutagenic, and carcinogenic compounds [1]. A major concern is the presence of high concentrations of synthetic dyes, which are typically non-biodegradable and disrupt aquatic ecosystems by inhibiting photosynthesis [2]. From both environmental and sustainability perspectives, it is essential to develop efficient dye separation and wastewater treatment processes that enable resource recovery while minimizing ecological damage [3,4]. Thus, appropriately dealing with this issue can improve water quality and contribute to a more sustainable textile production cycle.

Membrane technology has recently gained increasing importance in the treatment of textile wastewater due to its high separation efficiency, operational simplicity, and scalability [5,6]. Among available options, ceramic membranes have drawn considerable attention for their low fouling tendency, robust mechanical resistance, superior thermal and chemical stability, and long service life. However, their widespread adoption is hindered by high production costs, primarily due to the use of expensive industrial oxides such as alumina, silica, zirconia, and titania [7–10]. Additionally, ceramic membrane fabrication typically requires high sintering temperatures (above 1600 °C), which substantially increases energy consumption [11].

Therefore, identifying alternative, cost-effective raw materials is crucial for developing economically viable membranes to meet the growing demand for efficient water treatment solutions [12,13].

Ongoing research focuses on reducing the cost of both the porous support and the selective layer of ceramic membranes [9], with particular attention to the use of inexpensive raw materials, including geomaterials. Various studies have highlighted the potential of geomaterials, such as clays, kaolinite, perlite, peridotite, pyrophyllite, and others, for fabricating low-cost ceramic membranes [14]. For example, *El Ouaddari et al.* successfully employed a pozzolan support to develop an ultrafiltration (UF) membrane layer using purified clay [15]. The membrane achieved 99.0% rejection of direct red 80 (DR80) dye while maintaining high permeate flux. Similarly, *Boulkrinat et al.* fabricated a low-cost UF membrane supported by quartz sand and calcite, which demonstrated excellent protein rejection rates of up to 97.8% [16]. In another work, *Ben Ali et al.* utilized Tunisian kaolino-illitic clay to prepare a ceramic UF membrane [17]. The resulting membrane demonstrates high permeability for both gas and water, further highlighting the potential of geomaterials in the fabrication of low-cost ceramic membrane.

Among these materials, pyrophyllite has gained attention due to its natural abundance, layered silicate structure, thermal stability, and relatively low sintering temperature, making it a promising candidate for ceramic membranes. Membranes fabricated with pyrophyllite clay show some advantages compared to polymeric membranes, since the former can withstand harsher conditions by offering better chemical resistance and reduced fouling, while ensuring low-cost production. Furthermore, they are suitable for membrane anaerobic bioreactor systems, providing an efficient and eco-friendly alternative for the treatment of wastewater [18,19]. However, like many natural clays, raw pyrophyllite contains impurities such as quartz, amorphous silicates, carbonates, and organic matter that can adversely affect membrane

performance if not properly removed. These impurities may degrade the membrane mechanical strength and pore structure, thus impairing the separation performance of the membrane [16]. Although carbonates and organic matter in raw clay can enhance porosity and permeability, their excess can lead to oversized pores and cracking, especially in thin layers that are sensitive to thermal processing [15]. In contrast, amorphous silicates may vitrify at low sintering temperatures, closing pores and reducing membrane permeability [20]. Thus, impurities in natural clays can hinder membrane performance, making the adequate purification of clay a critical step in the fabrication of high-performance membranes [15].

This work proposes an UF ceramic membrane made with purified pyrophyllite for the treatment of dye-contaminated water. The raw pyrophyllite underwent a series of physicochemical purification steps, including sedimentation, carbonate removal, and elimination of organic matter, to optimize the process and improve its suitability for membrane production. The properties of the purified pyrophyllite are thus presented to evaluate its potential as a membrane precursor. Membranes were fabricated using pyrophyllite at various stages of purification to investigate how each treatment step influences membrane performance. Sintering was performed at temperatures between 1000 and 1100 °C to refine the structural and functional attributes of the membrane. The resulting membrane properties are discussed in terms of permeability, dye rejection, and fouling resistance. Furthermore, a preliminary cost analysis is presented out to evaluate the economic feasibility of the optimized membrane.

2. Materials and methods

2.1. Materials

Natural pyrophyllite was extracted from the Gunfouda Region of Morocco. Polyvinyl alcohol granular powder (PVA, Bulk density: 610-650 Kg m^{-3}) was provided by Alquera. Methylene blue (MB, ≥ 95 wt%)) was purchased from Loba Chemie. Direct red 80 (DR80, ≥ 25 wt%) was sourced from Alfa Aesar. Congo red (CR, ≥ 35 wt%) and hydrochloric acid (HCl, 37 wt%)

were purchased from Sigma-Aldrich. Additional characteristics of the dyes are listed in **Table 1**. Hydrogen peroxide (H_2O_2, 35%) was provided by Riedel-de Haën. Distilled water was used for solution preparation and filtration experiments. The flat ceramic support was prepared using raw pyrophyllite through a dry pressing method and sintered at 1150 °C. Its detailed characteristics are given in **Table 2** [5].

Table 1. Main characteristics of DR80, CR and MB dyes.

Dye	Molecular formula	Molecular weight (g mol^{-1})	Charge	pK	Wavelength λ_{max} (nm)	Chemical structure
DR80	$C_{45}H_{26}N_{10}Na_6O_{21}S_6$	1373.09	anionic	-	528	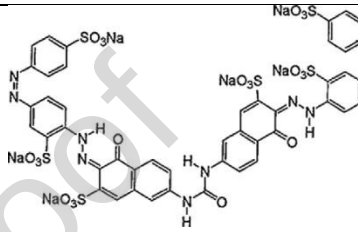
CR	$C_{32}H_{22}N_6Na_2O_6S_2$	696.63	anionic	3.5 - 5.5	497	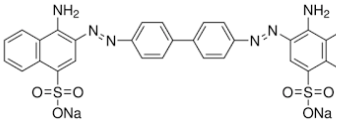
MB	$C_{16}H_{18}ClN_3S$	319.85	cationic	2.6 - 11.2	663	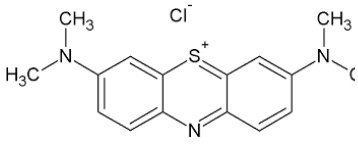

Table 2. Main characteristics of the flat pyrophyllite support.

Parameter	Value
Porosity (%)	21.7
Average pore size (µm)	0.80
Flexural strength (MPa)	17.7
Permeability (L m^{-2} h^{-1} bar^{-1})	154
Diameter (mm)	40
Thickness (mm)	2

2.2. Purification of the pyrophyllite

The pyrophyllite clay was purified by adopting a series of physicochemical treatments, which included sedimentation, removal of carbonates, and removal of organic matter. The purification procedure is schematically depicted in **Fig. 1.**

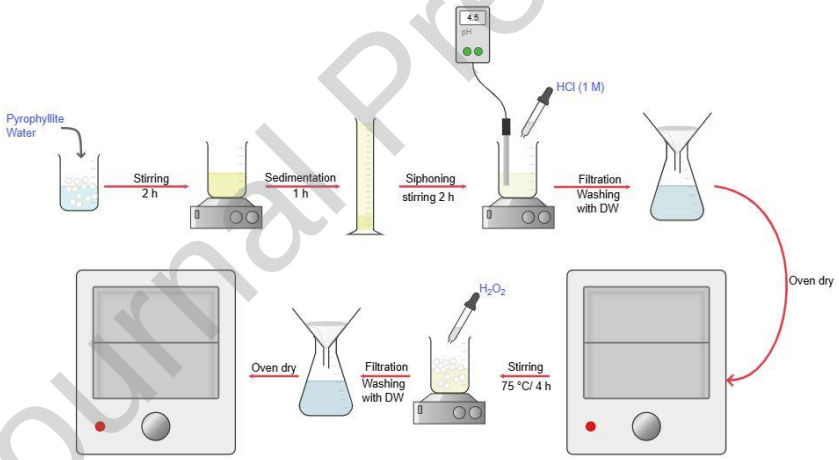

Fig. 1. Scheme of the purification process of pyrophyllite clay.

2.2.1. Sedimentation

The raw pyrophyllite was ground and sieved through a 63 µm mesh to obtain a uniform powder. The powder was then mixed with water and continuously stirred for 2 h. To recover the pyrophyllite phase, the suspension was placed into a glass tube, allowing heavy particles to settle for 1 h. The remaining suspension was then centrifuged at 3000 rpm for 20 min, and the obtained solid phase was collected and dried at 100 °C.

2.2.2. Removal of carbonates

To remove carbonates, a sub-sample of the pyrophyllite clay was dispersed in water, followed by the gradual addition of a 0.1 M HCl solution, while maintaining the pH at 4.5 to preserve the integrity of the clay minerals. The slurry was stirred slowly for 2 h to ensure complete decomposition of carbonates. Afterward, the sample was rinsed with water and centrifuged until the supernatant was clear and free of chloride [15].

2.2.3. Removal of organic matter

Organic matter was removed by oxidation on one of the samples following the removal of carbonates. In detail, 35% H_2O_2 was added to the sample to oxidize and decompose the organic matter into CO_2 and water-soluble byproducts, without affecting the pyrophyllite clay. The slurry was stirred and heated in the presence of H_2O_2 at 75 °C for 4 h. Afterwards, the solid phase was separated by centrifugation, rinsed with water, and dried at 100 °C for 24 h.

2.3. Preparation of purified pyrophyllite membrane

Various membranes were prepared deploying different pyrophyllite clays, each pre-treated through a specific purification sequence and then deposited on a flat pyrophyllite support (**Table 3**). Firstly, a suspension containing 3 wt% of purified pyrophyllite, 0.6 wt% of PVA, and water was prepared and mixed under continuous stirring. The flat pyrophyllite support was then coated with the suspension by applying vacuum filtration process. Subsequently, the membrane was dried overnight at room temperature. Thereafter, the membrane was heated to plateau temperature of 300 °C for 2 h to eliminate the entrapped PVA. Finally, it was sintered for 2 h at different sintering temperatures ranging from 1000 to 1100 °C.

Table 3. Experimental conditions of the purified pyrophyllite membranes.

Membranes	**Purification steps**	**Sintering temperature (°C)**
S1050	Sedimentation (S)	1050
SC1050	Sedimentation- Removal of carbonates (SC)	1050

SCO1050	Sedimentation- Removal of carbonates - Removal of organic matter (SCO)	1050
SC1000	Sedimentation- Removal of carbonates (SC)	1000
SC1100	Sedimentation- Removal of carbonates (SC)	1100

2.4. Filtration experiment

Cross-flow filtration tests were carried out using a stainless steel UF setup detailed elsewhere [15]. The membrane was inserted into the membrane housing with an effective surface area of 5.30 cm^2, and a pump was used to circulate the feed solution in the filtration system. The water permeability, L_p (L m^{-2} h^{-1} bar^{-1}), of the membrane sample was determined by measuring the permeate flux, J_w (L m^{-2} h^{-1}), as a function of transmembrane pressure, ΔP (bar), which was adjusted from 0 to 3 bar using an expansion valve. **Eqs. (1–2)** were used to calculate flux and permeability, respectively.

$$J_W = \frac{V}{A \times t} \quad \textbf{(1)}$$

$$L_P = \frac{J_W}{\Delta P} \quad \textbf{(2)}$$

where A (m^2) is the effective membrane area, t (h) is the filtration time, and V (L) is the volume of permeate collected at each respective time. Filtration of DR80 (50 ppm, pH = 5.47), MB (50 ppm, pH = 4.56), and CR (50 ppm, pH = 7.11) using the optimized membrane was performed at a transmembrane pressure of 3 bar for 2 h. The rejection (%) of the dye was calculated according to **Eq. (3)**.

$$R = \frac{C_f - C_P}{C_f} \times 100 \quad \textbf{(3)}$$

Where C_p and C_f represent the dye concentration in the permeate and feed solutions, respectively.

2.5. Fouling tests

The fouling behavior of the optimized membrane was assessed as described by *Essate et al.* [4]. Briefly, water was filtered through a virgin membrane to measure the initial water flux, J_{w0}, and

then a DR80 solution (50 ppm) was filtered to measure the flux in the presence of the dye, J_{dye}. Following this step, the membrane was removed from its housing, cleaned for 30 min in an ultrasonic bath, and then again employed for water filtration to determine the water flux upon cleaning, J_{w1}. Four fouling parameters, namely, the flux recovery ratio (FRR), total flux decline ratio (TFR), reversible flux decline ratio (RFR), and irreversible flux decline ratio (IFR), were calculated using **Eqs. (4–7)**:

$$FRR = \frac{J_{W1}}{J_{W0}} \times 100 \quad \textbf{(4)}$$

$$TFR = (1 - \frac{J_{dye}}{J_{W0}}) \times 100 \quad \textbf{(5)}$$

$$RFR = \left(\frac{J_{W1} - J_{dye}}{J_{W0}}\right) \times 100 \quad \textbf{(6)}$$

$$IFR = \left(\frac{J_{W0} - J_{W1}}{J_{W0}}\right) \times 100 \quad \textbf{(7)}$$

2.6. Characterizations of the materials

The pyrophyllite clay chemical composition was analyzed using X-ray fluorescence (XRF) (Axios-Panalytical). Free carbonates were obtained based on Bernard calcimeter method. Free carbonates were determined using the Bernard calcimeter method. In this method, the carbonates in the sample react with HCl, and the CO_2 evolved from carbonate decomposition was measured, allowing for the quantification of the carbonate content in the sample. Crystalline phases were identified using a Panalytical X'Pert PRO X-ray diffractometer with CuK_α radiation (1.5418 Å). Fourier transform infrared spectroscopy (FTIR) was performed from 4000 to 400 cm^{-1} using a Bruker spectrometer (Vertex 70) to analyze the molecular structure of the materials. A 20 kV Quattro S FEI scanning electron microscope (SEM) was used to visualize the morphology of the membrane. ImageJ software (v.1.53a) was used to calculate the average particle size of the membrane based on SEM images and analyzing >100 particles [21]. The zeta potential analyzer, Litesizer 500, was used to determine the charge of the purified pyrophyllite membrane as a function of pH using water. The average pore size (d)

of the membrane active layer was estimated according to the extended Hagen–Poiseuille (**Eq. (8)**) [22].

$$d = 2\sqrt{8J_w \times \delta \times \frac{\tau}{\varepsilon} \times \frac{\Delta X}{\Delta P}} \quad \textbf{(8)}$$

where J_w is the water flux (m s^{-1}), δ is water viscosity (8.9×10^{-4} Pa s), τ is the tortuosity factor, ΔX is the thickness of the membrane layer (m), ΔP is the transmembrane pressure (Pa), while ε presents the membrane porosity (%). The concentration of dyes was determined using a JASCO V-730 spectrophotometer and the wavelength of peak light absorption is indicated in **Table 1**.

3. Results and discussion

3.1. Characteristics of the pyrophyllite clay

3.1.1. Chemical composition

Table 4 reports the chemical composition of the raw pyrophyllite and purified pyrophyllite. The raw pyrophyllite predominantly consisted of 63.13 wt% SiO_2 and 26.94 wt% Al_2O_3, alongside small amount of K_2O (3.40 wt%). The SiO_2/Al_2O_3 mass ratio, approximately 2.4, indicates a substantial presence of quartz and/or amorphous silica [5]. Moreover, the main oxides, SiO_2 and Al_2O_3, were structurally associated with quartz and muscovite, which commonly exist in natural pyrophyllite [5]. The loss on ignition (LOI) at 1000 °C can be attributed to the decomposition of carbonates and organic matter, and to a lesser extent to the dihydroxylation of clayey minerals. These phenomena were confirmed with the Bernard calcimeter method, revealing a value of 4.16 wt% of carbonate content in the raw pyrophyllite [15]. On the other hand, the purified pyrophyllite exhibited significant changes in its oxide composition, with a reduction in SiO_2 and an increase in Al_2O_3 contents. This was confirmed by the decrease of SiO_2/Al_2O_3 ratio to approximatively 2, indicating the reduction of SiO_2 in the purified simples. The LOI of purified pyrophyllite insignificant, which suggests that the high LOI of raw pyrophyllite may be primarily attributed to decomposition of carbonates.

Table 4. Chemical composition of raw and purified pyrophyllite obtained at different purification steps.

Oxides	SiO_2	Al_2O_3	K_2O	TiO_2	P_2O_5	SO_3	SrO	Fe_2O_3	Na_2O	CaO	BaO	MgO	LOI*
Raw pyrophyllite (wt%)	63.13	26.94	3.40	0.39	0.40	0.07	0.28	0.31	0.11	0.18	0.17	0.27	4.25
S (wt%)	62.02	31.58	3.15	0.03	0.77	0.06	1.01	0.33	0.23	0.10	0.46	0.14	0.11
SC (wt%)	62.81	30.52	3.89	0.06	0.92	0.03	0.97	0.23	0.15	0.07	0.12	0.16	0.07
SCO (wt%)	63.01	30.17	3.83	0.09	0.46	0.04	0.66	0.27	0.14	0.09	0.08	0.11	0.03

*Loss of ignition at 1000 °C.

3.1.2. Crystalline structure of the pyrophyllite clay

XRD patterns of both raw and purified pyrophyllite at different purification degrees are shown in **Fig. 2**. The raw material predominantly contained pyrophyllite ($Al_2Si_4O_{10}(OH)_2$), with small quantities of quartz (SiO_2) and muscovite [$K(Al_2)(AlSi_3O_{10})(OH)_2$] [23,24]. It is worth mentioning that no crystalline carbonate phase was detected, suggesting that the carbonates might exist in trace-level and/or in an amorphous form. After sedimentation and carbonate removal, the characteristic peaks of pyrophyllite increased, while those of quartz and muscovite slightly reduce, indicating that the purification removed some of the associated minerals, resulting in prominent pyrophyllite peaks. Finally, the organic matter removal step further intensified the pyrophyllite peaks, suggesting enhanced purity. Overall, the purification process effectively enriched pyrophyllite and eliminated impurities [25].

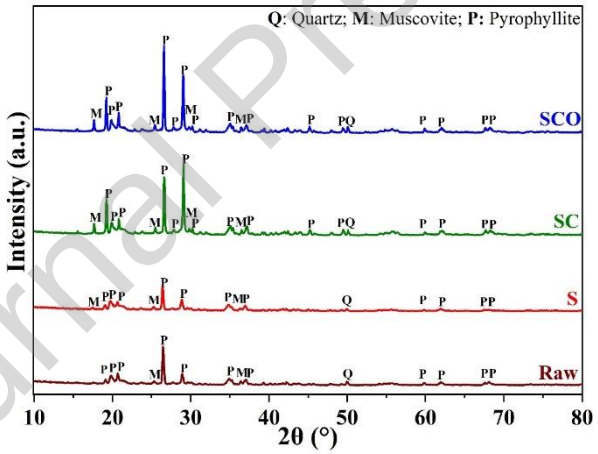

Fig. 2. XRD patterns of raw and purified pyrophyllite at different purification steps.

3.1.3. Molecular structure of the clay

FTIR spectra of raw and purified pyrophyllite at different purification steps are presented in **Fig. 3**. For the raw pyrophyllite, the bands observed at 942 and 3673 cm^{-1} can be attributed to OH vibrations and Al_2OH elongation [26]. The bands between 1119 and 986 cm^{-1} are attributed to the Si-O vibrations, characteristic of aluminosilicate, while the band found at 833 is attributed to Si-O bond vibrations in quartz phase [27]. Additionally, the bands at 514 and 441 cm^{-1} correspond to the deformation vibrations of Si-O and Si-O-Al bonds, which are characteristic

of clay minerals [28]. After purification, the band particularly at 3673 cm^{-1} (OH vibrations) became slightly intense. This observation indicates that the purification process removed impurities without affecting the core aluminosilicate structure.

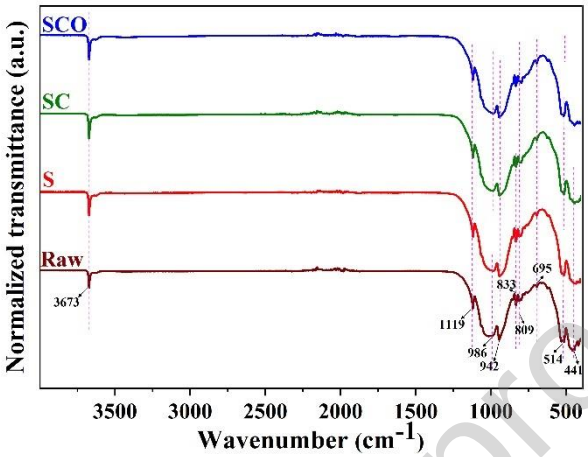

Fig. 3. Normalized FTIR spectra of raw and purified pyrophyllite following different purification steps.

3.1.4. Morphology of the clay

SEM micrographs of raw and purified pyrophyllite samples are shown in **Fig. 4**. The raw pyrophyllite particles exhibited irregular shapes and non-uniform sizes, with an average size of approximately 11.70 µm (**Fig. 4a**). After the sedimentation step (**Fig. 4b**), most of the large impurities were removed, reducing the particle size to roughly 1.79 µm, thus resulting in particles with more uniform shape and smaller size compared to the raw pyrophyllite. After decarbonation and organic matter removal, the particles appeared more resolved and morphologically differentiated, with their size reducing to approximately 1.35 µm after decarbonation and slightly further decreasing to 1.14 µm upon organic matter removal (**Fig. 4c and Fig. 4d**). This observation implies that the purification processes effectively removed larger impurities [29], leading to a considerable reduction in particle size and improvement in particle uniformity.

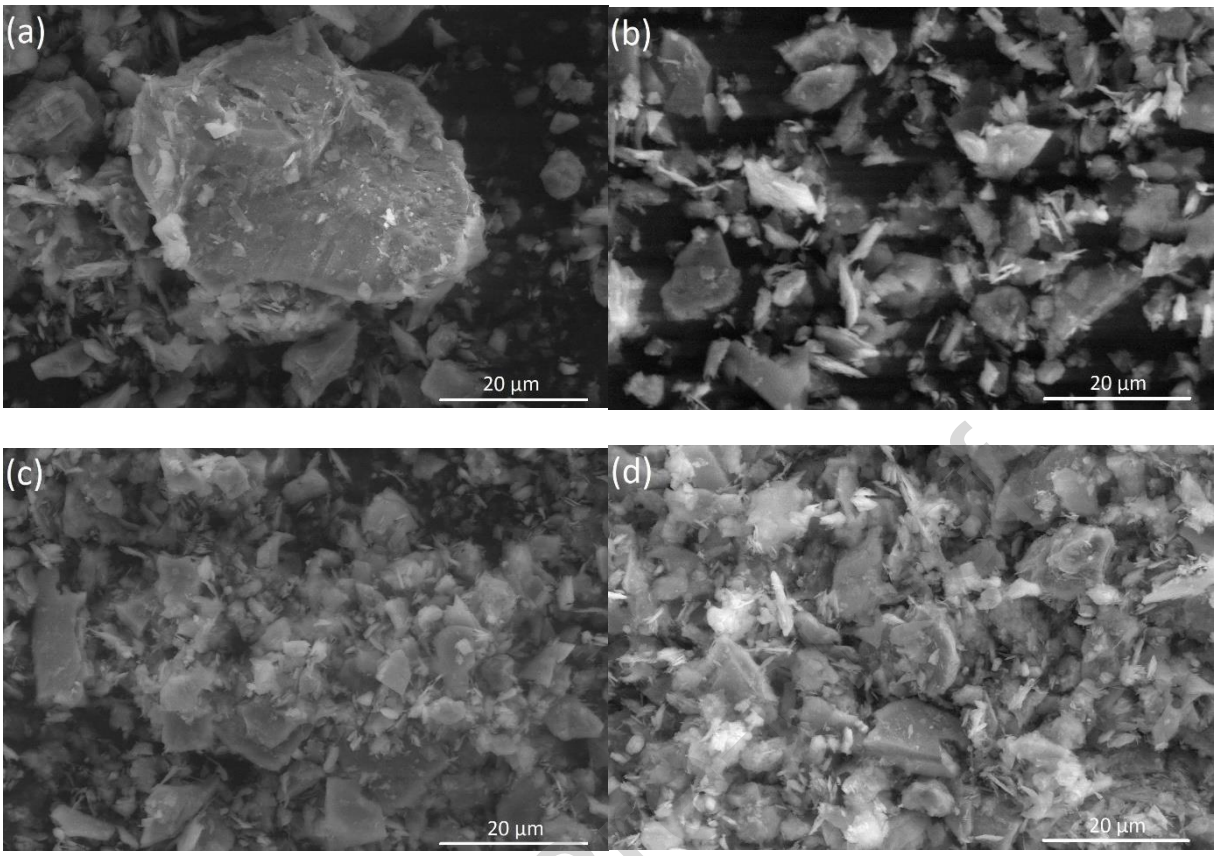

Fig. 4. SEM micrographs of (a) raw pyrophyllite, and purified pyrophyllite after (b) sedimentation, (c) removal of carbonates and (d) removal of organic matter.

3.2. Effect of purification steps on morphology and performance of the UF membrane

3.2.1. Membrane morphology

Fig. 5 presents the top-surface and cross-sectional views of the fabricated purified pyrophyllite membrane produced with pyrophyllite subject to different purification steps. The top-surface images reveal that membranes were uniformly covered with purified pyrophyllite, with the absence of cracks or any other obvious defects. The morphology appears relatively uniform, with well distributed pore size. **Fig. 5a** shows S1050 membrane, which exhibited larger particles on the surface, mainly caused imperfect purification. In contrast, **Fig. 5b** and **Fig. 5c** present SC1050 and SCO1050 membranes, whereby the particles were more uniformly distributed, contributing to a smoother surface texture and more consistent pore size [5]. The cross-sectional view in **Fig. 5d** corresponding to SC1050, indicates adequate adhesion between

the active layer and the support. This apparently seamless structure may be attributed to the embedding of the membrane active layer within the support surface pores and surface features, also owing to a suitable surface roughness and to the use of the same material for both active and support layers [30]. The membrane active layer had an approximate thickness of 11.80 μm, smaller than those typically found in the literature. In summary, suitable purification was important to the preparation of membranes with uniform surface structure, such as SC1050 and SCO1050, since it guarantees consistent particle distribution and reduces defects.

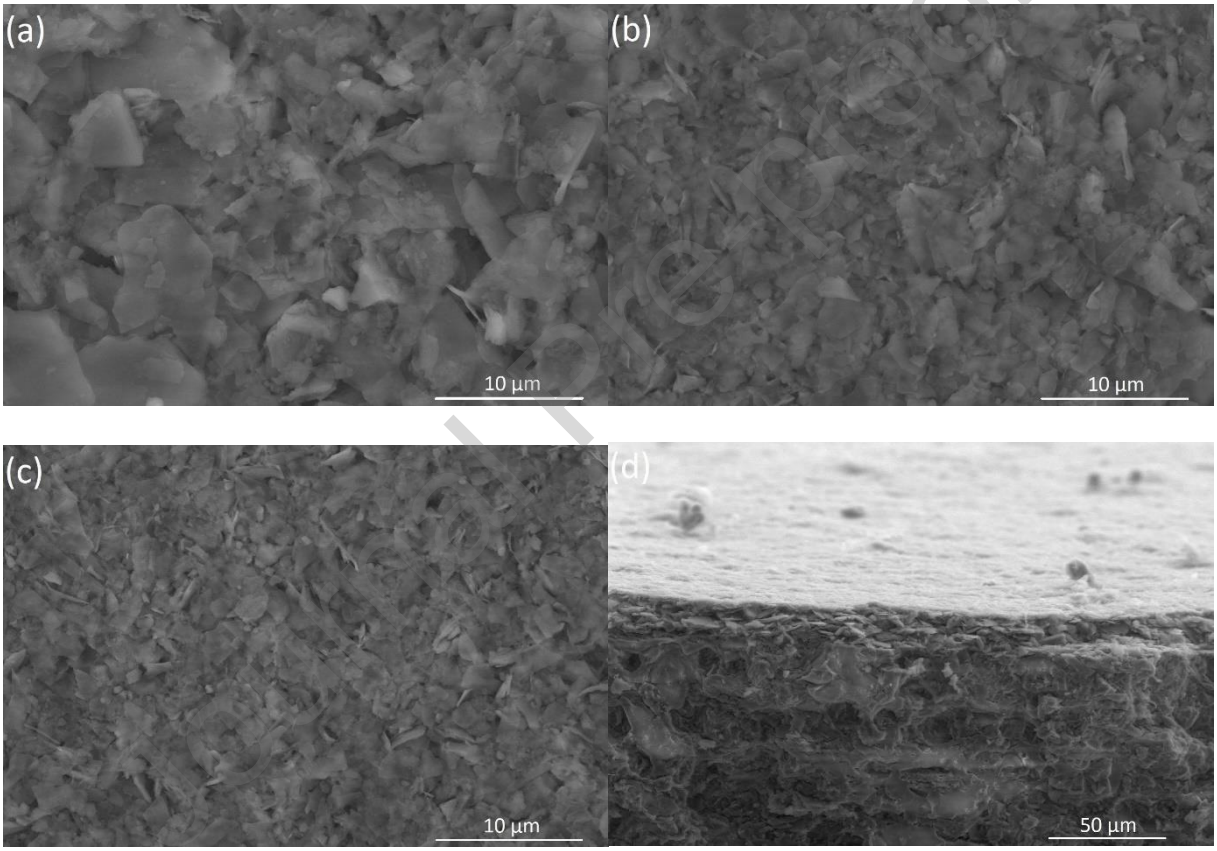

Fig. 5. SEM micrographs of top surface: S1050 (a), SC1050 (b), SCO1050 (c), and cross-section of SC1050 (d).

3.2.2. Membrane pore size

The pore size of the UF membrane is a crucial factor that affects its separation efficiency. UF-range pores offer an effective solution for the removal of macromolecules and some dyes from wastewater [31]. Indeed, the purification of pyrophyllite could impact the pore size of the

resulting membrane [15,29]. **Fig. 6a** shows the estimated, average pore diameter of the purified pyrophyllite membrane obtained with different purification steps. S1050, SC1050 and SCO1050 membranes exhibited pore sizes of approximately 69, 44 and 40 nm, respectively. These values imply that all membranes fell within the UF range [32,33]. S1050 membrane displayed the largest pore size (69 nm), which may be attributed to the predominance of larger particles and the insufficient presence of finer particles to enhance compaction of the membrane layer during sintering [34]. SC1050 membrane exhibited a reduced pore size; while carbonates removal may generate additional voids in the particle structure, it also aid particle packing, resulting in a more optimal pore size [35]. Finally, SCO1050 membrane showed the smallest pore size (40 nm), consistent with SEM observations that revealed a smoothly packed structure.

3.2.3. Surface zeta potential

Fig. 6b illustrates the trend in zeta potential as a function of pH for S1050, SC1050 and SCO1050 membranes. All membranes maintained a relatively stable, negative, surface charge across the pH range of 2–7, indicating the likely protonation and deprotonation of aluminum hydroxyl groups (-Al-OH), forming -Al-O^- in basic medium and Al-OH_2^+ in acidic [36]. The more purified pyrophyllite produce active layers that were characterized by slightly more negative values of the zeta potential, especially those produced with pyrophyllite following oxidation of organic matter. This observation may be attributed to a smaller amount of material interfering with the charges provided by the aluminum hydroxyl groups. Only with S1050 membrane, a marked drop of the zeta potential to −33.1 mV was observed at pH = 10, a phenomenon not observed with the other two membranes obtained with clay subjected to decarbonation. Therefore, it is possible that carbonate ions are responsible for the more negative value of zeta potential above neutral pH [37].

3.2.4. Water flux of the membranes

The water flux of the purified pyrophyllite membranes is presented in **Fig. 6c**. The flux curves exhibited a linear behavior, indicating that Darcy's law was verified [30]. S1050 membrane exhibited the highest permeability (113 L m^{-2} h^{-1} bar^{-1}), likely due to its larger pore size **(Section 3.2.2)**, which facilitated water permeation. SC1050 membrane showed a moderate permeability of 86 L m^{-2} h^{-1} bar^{-1}, while SCO1050 exhibited a permeability of 73 L m^{-2} h^{-1} bar^{-1}, likely due to the more compact structure following carbonate and organic matter removal, which also resulted in smaller surface pores [38]. Notably, all obtained permeability values fell within the UF range [39]. It should be mentioned that the fabricated membranes exhibited a good flexural strength thanks to the pyrophyllite support (**Table 2**) that could support hydraulic pressures applied UF applications.

3.2.5. Dye filtration experiment

The impact of purification steps on membrane filtration performance using DR80 solution is illustrated in **Fig. 6d**. The flux demonstrated a progressive decline after each purification step. Specifically, S1050 membrane displayed a flux of approximately 130.1 L m^{-2} h^{-1} , which decreased to 101.9 L m^{-2} h^{-1} for SC1050 membrane, and 96.8 L m^{-2} h^{-1} for SCO1050, consistent with permeability values and with the structural and pore size characteristics [15]. The removal of impurities reduced voids, leading to a more compact and homogeneous membrane. Accordingly, the dye rejection of S1050 membrane was the lowest (71.0%), improving with purification intensity, reaching 91.4% for SC1050 membrane and further increasing to 92.1% for SCO1050 membrane. This enhancement may also be linked to reduced pore size. Dye rejection is likely influenced by the electrostatic repulsion, since the membrane surface exhibited a negative charge, causing repulsion of the negatively charged DR80 dye [30]. The similar rejection rates of SC1050 and SCO1050 suggest that decarbonation played a key role in optimizing membrane selectivity, while organic matter removal had a minor influence [40]. Based on the results obtained, SC1050 membrane was selected to study the effect of

sintering temperature, owing to its improved behavior compared to S1050 membrane. However, since SC1050 membrane exhibited similar characteristics to SCO1050 membrane, its selection goes in the direction of minimizing the preparation steps and the cost of the membrane fabrication.

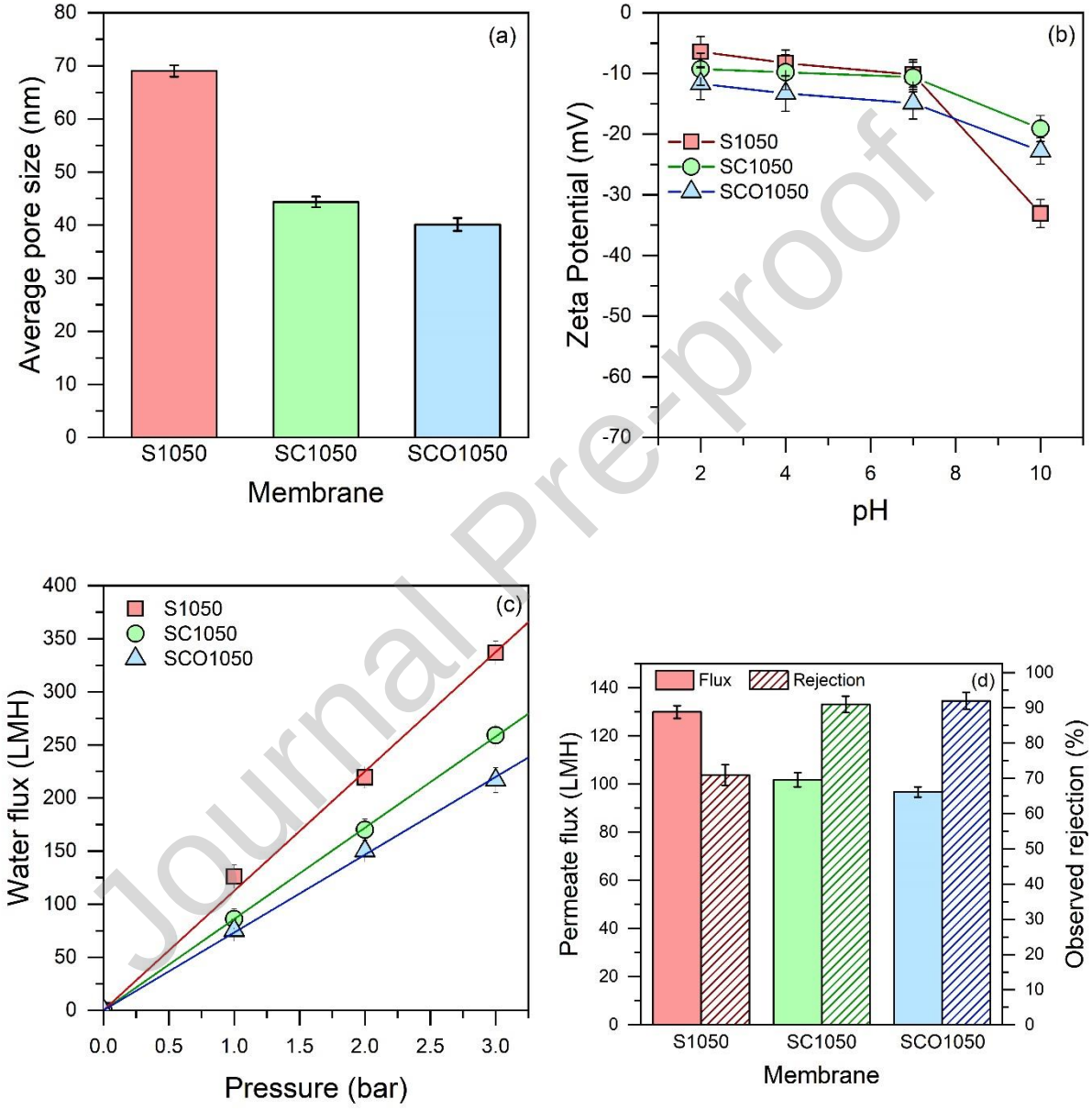

Fig. 6. The effect of different purification steps of pyrophyllite on (a) Membrane pore size, (b) Zeta potential of the membranes as a function of pH, (c) Water flux of the membranes as a function of transmembrane pressure, (d) Permeate flux and rejection of DR80.

3.3. Effect of sintering temperature on morphology and performance of the UF membrane

3.3.1. Membrane morphology

SEM micrographs of purified pyrophyllite membranes sintered at different temperatures, from 1000 to 1100 °C, are shown in **Fig. 7**. SC1000 membrane exhibited relatively large pores and loosely bonded particles, indicating insufficient sintering (**Fig. 7a**), which may compromise the filtration performance [5]. As the temperature increased to 1050 °C (**Fig. 7b**), the particles appeared to merge, enhancing grain connectivity and leading to smaller, more uniform pores [10]. At 1100 °C (**Fig. 7c**), SC1100 membrane underwent apparent densification, likely due to stronger interparticle cohesion but an increase in pore size [12]. Excessive melting at high temperature may induce pore enlargement, which could negatively impact filtration performance by decreasing the selectivity [14].

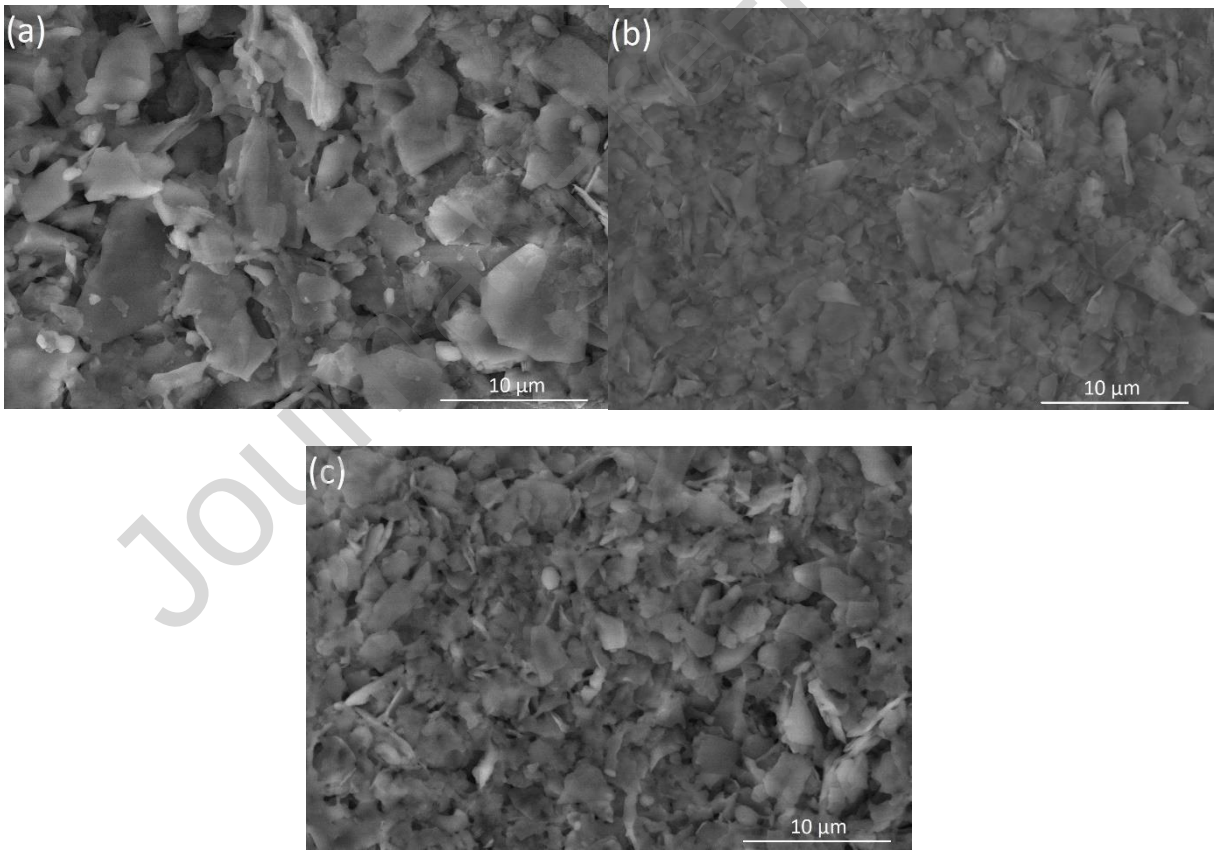

Fig. 7. SEM images of SC1000 (a), SC1050 (b) and SC1100 (c).

3.3.2. Membrane pore size

The influence of sintering temperature on pore size was investigated to better understand its effect on the structural properties of purified pyrophyllite-based membrane. The results indicate that sintering temperature played a role in determining pore size. Data summarized in **Fig. 8a** shows that the pore size of SC1000 was 66 nm, which decreased to 44 nm for SC1050. This reduction may be attributed to the sintering process itself, which promotes particle bonding and densification, resulting in a more compact ceramic structure [10]. However, when the sintering temperature was further increased to 1100 °C (SC1100), the pore size increased again to 49 nm, likely due to pore restructuring caused by coalescence phenomena [41].

3.3.3. Surface zeta potential

Fig. 8b presents the zeta potential behavior of the purified pyrophyllite membranes. No substantial difference in general behavior was observed for the three membranes obtained at different sintering temperatures, all characterized by slightly negative zeta potential that declines smoothly in alkaline solutions [36]. Note that the sintering process can reduce the density of functional groups, such as –OH [42]. Slight differences in the observed potential at pH = 10 for the three membranes may thus be attributed to the different nature and extent of the sintering process, whereby greater resulting porosity and lower densification level somewhat correlates with a potential of larger negative magnitude.

3.3.4. Water flux of the membranes

The measured water flux of purified pyrophyllite membranes is summarized in **Fig. 8c**. The permeate flux as a function of transmembrane pressure was again found to be linear. The water permeability decreased from 110 to 86 L m^{-2} h^{-1} bar^{-1}, when the sintering temperature increased from 1000 to 1050 °C. This drop is mainly attributed to the reduction in pore size at higher temperatures [42]. The decline in permeability can also be explained with the overall densification of the membrane matrix and/or partial vitrification of clay materials that contributed to pore closure [10]. The permeability slightly increased to 90 L m^{-2} h^{-1} bar^{-1} for

SC1100 membrane, consistent with the morphological and pore size discussions reported in **Section 3.3.2** [41].

3.3.5. Dye filtration experiment

The effect of sintering temperature on the dye filtration performance of purified pyrophyllite membrane is illustrated in **Fig. 8d**. The flux in the presence of dye decreased from 123.8 to 101.9 L m^{-2} h^{-1}, when the sintering temperature increases from 1000 to 1050 °C. This decline could be attributed to reduced pores [43]. However, the flux stabilized between 1050 and 1100 °C, likely because the pore sizes of SC1050 and SC1100 membranes were relatively similar [44]. On the other hand, SC1050 membrane showed the highest dye rejection of 91.4%, likely due to its improved integrity and pore homogeneity, indicating that sintering at 1050 °C optimally balances permeability and selectivity [4]. These findings align well with those discussed in **Section 3.3.2**.

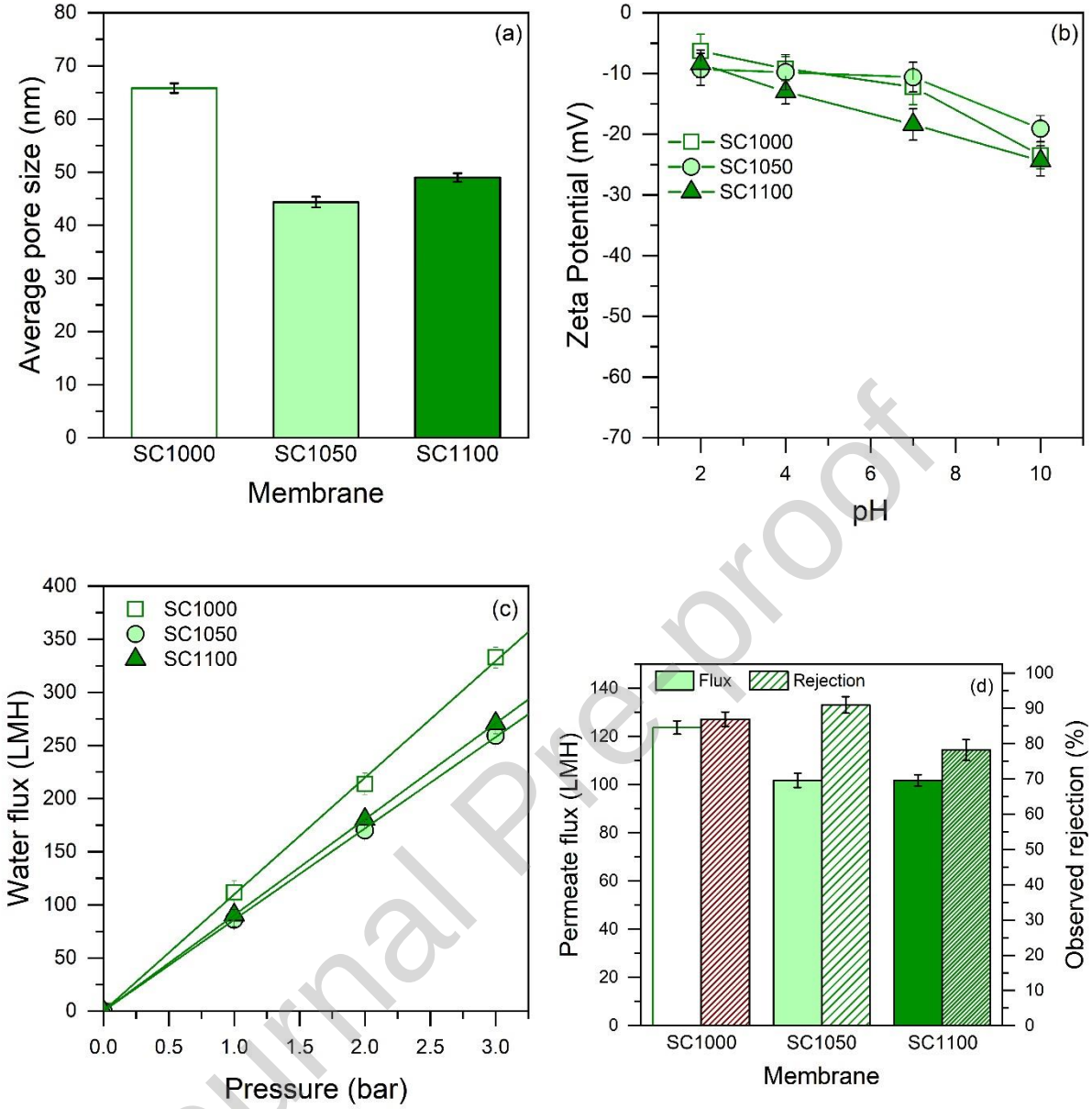

Fig. 8. Effect of sintering temperature on (a) membrane pore size, (b) Zeta potential of purified pyrophyllite membrane, (c) permeability of purified pyrophyllite membrane and (d) permeate flux and rejection of DR80.

3.4. Separation performance of the optimized purified pyrophyllite membrane

The performance of SC1050 membrane in terms of flux and selectivity was evaluated by also filtering CR and MB dye solutions at a concentration of 50 ppm under a pressure of 3 bar for 2 h. The results are compared with those obtained with DR80 dye to assess the effect of molecular weight and dye charge on membrane performance. **Fig. 9a** presents the observed flux measured

with the three solutions. The fluxes of DR80 and CR remained stable throughout filtration. The observed difference in flux between these dyes might be partly attributed to differences in molecular size, as the molecular weight of DR80 is twice as high as that of CR and substantially higher than that of MB. Consequently, DR80 molecules may accumulate more easily at the membrane-solution interface and within the surface pores, thus hindering mass transport. Concentration polarization is common in pressure-driven membrane processes and can slightly disrupt flux without causing irreversible fouling [45] [4]. **Fig. 9b** presents the dye rejection performance of SC1050 membrane, showing a distinct difference between DR80 (pH = 5.47) and CR (pH = 7.11), with rejection rates of 91.4 and 81.4%, respectively. This disparity can be attributed to the dye chemical structure and molecular weight. Notably, the membrane exhibited a negative surface charge in the studied pH range from 2 to 10 [46]. During DR80 and CR filtration, the negative membrane charge likely repelled the anionic dyes, enhancing the rejection and suggesting that the rejection of DR80 and CR is at least partly driven by the electrostatic mechanisms [47]. The high rejection of DR80 may result from both its higher charge density and its larger molecular size. As for MB (pH = 4.56), a cationic dye, the membrane achieved an apparent rejection of 92.9%. In this case, the positively charged dye was rejected by the negatively charged membrane surface, possibly due to adsorption mechanisms in earlier filtration times [30]. **Table 5** highlights the filtration parameters of some membranes reported in the literature, as well as their separation efficacy in the removal of dyes, providing a comparison with the purified pyrophyllite SC1050 membrane. Based on the comparison, SC1050 membrane presents balanced pore size compared to carboxylated poly (aryl ether nitrile) membrane (7.7 nm) [48], and the coated pyrophyllite (100 nm) characterized by larger pores [49]. This balance represents a compromise to reach high dye rejection with suitable permeability values.

Table 5. Comparison of water permeability and dye rejection of UF membranes, based on literature reports.

Membrane	Permeability (L m^{-2} h^{-1} bar^{-1})	Pore size (nm)	Dye	Dye concentration (ppm)	Rejection (%)	Reference
Purified clay	16.40	90	DR80	50	97	**[17]**
Polysulfone/ polystyrene	24	-	DR80 Methyl orange	50	91 76	[47]
Coated pyrophyllite membrane	590	100	MB Methyl orange	-	92.2 93.2	[49]
Carboxylated poly (aryl ether nitrile)	2.9	7.7	CR Evans blue n Coomassie brilliant blue	100	99.6 99.9 99.4	[48]
Zirconia	36	80	Acid orange 74	50	90	[50]
SC1050	85.9	44.3	DR80 CR MB	50	91.4 81.4 92.9	**This work**

3.5. Fouling behavior

Membranes gradually lose performance, with a decline in flux due to fouling that occurs within the membrane surface or within its pores [47]. To better understand this phenomenon, the fouling behavior of the SC1050 membrane was preliminarily evaluated by assessing fouling parameters during the filtration of a DR80 solution. **Fig. 9** presents the flux of DR80 solution, as well as water flux before and after dye filtration (**Fig. 9c**). The resulting fouling parameters,

including FRR, TFR, RFR and IFR, are shown in **Fig. 9d**. After dye filtration, the water flux did not fully recover to the initial value. This difference likely resulted from the blockage of membrane pores by some of the retained dye molecules [30]. FRR was 89.9%, suggesting that SC1050 membrane exhibited adequate fouling behavior in terms of recovery of productivity upon cleaning [4]. The TFR was found to be approximately 56.3%, likely due to pore blockage and the dye molecules accumulation on the surface of the membrane. This latter mechanism of fouling, caused by polarization layer formation, can be quantified by the RFR parameter of approximately 46.2%. In contrast, the irreversible fouling associated with pore blockage is represented by the IFR parameter, which was only about 10.1% [15]. It is worth noting that the membrane could be subjected to chemical cleaning to reduce IFR, as ceramic membranes as well as pyrophyllite material exhibit good chemical stability [18,19].

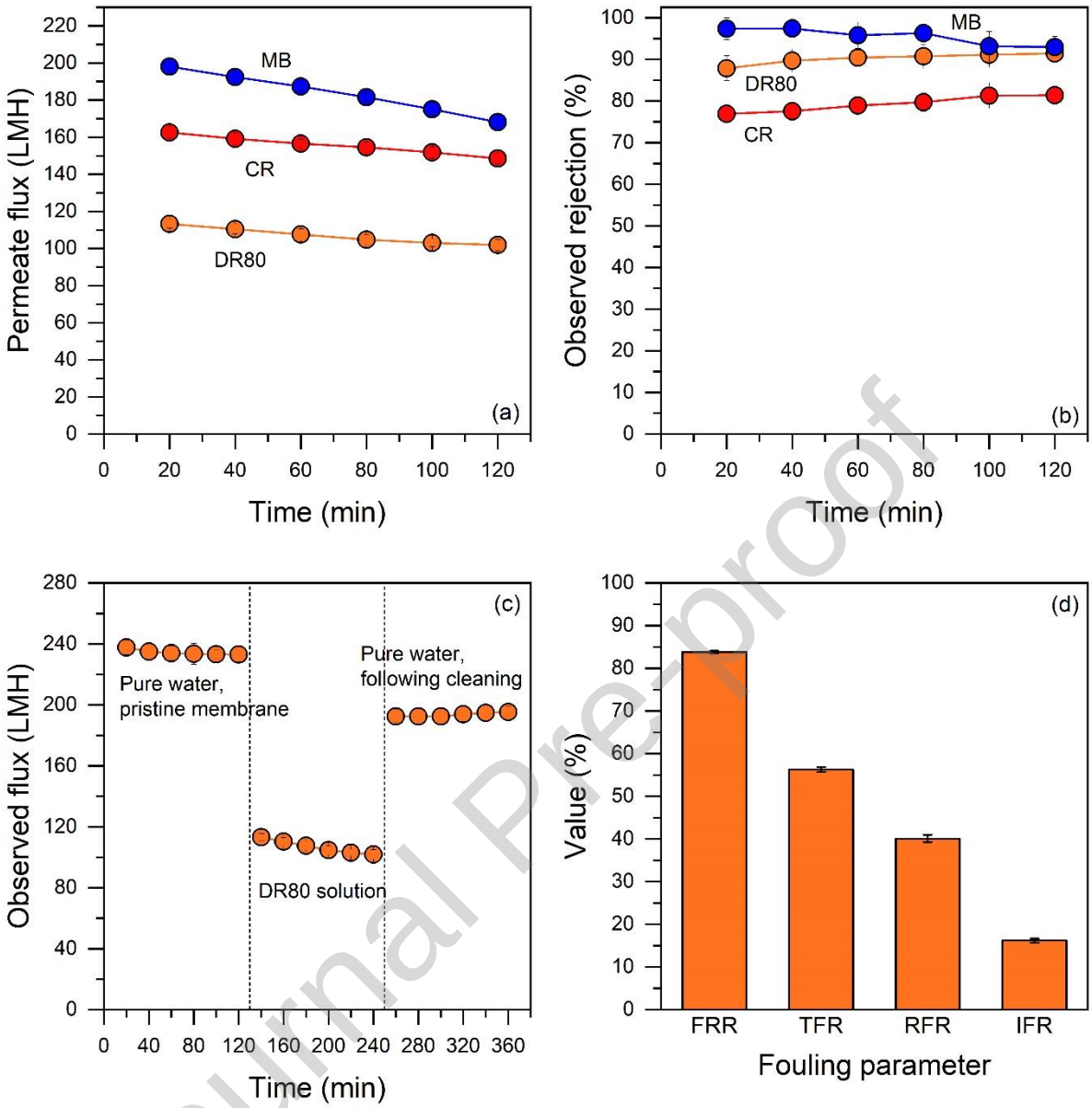

Fig. 9. (a) Permeate flux and (b) rejection of DR80, CR and MB dyes as a function of filtration time using SC1050 membrane. (c) Permeate flux observed with DR80 dye solution, as well as with water for a pristine membrane and a membrane after dye removal and physical cleaning, (d) Resulting fouling parameters of the membrane.

3.6. Cost estimation

A preliminary cost estimation of the optimized membrane (SC1050) was performed based only on the unit prices of raw materials and energy consumed during fabrication. Details of raw

material and energy costs are provided in **Table 6**, and are calculated, respectively, using **Eqs. (9-10)** [51].

$$C_{material} = \frac{\text{weight product}_{raw} \times (\text{Used percentage} \times \text{Unit Price}_{raw})}{\text{Unit area}} \quad \textbf{(9)}$$

$$C_{energy} = \frac{\text{Operating time} \times \text{Power} \times \text{Unit charge}}{\text{Unit area}} \quad \textbf{(10)}$$

The total membrane cost includes the expenses for the ceramic pyrophyllite support and the purified pyrophyllite layer. The support fabrication was evaluated at USD 6.14 m^{-2}, which is considerably lower than the typical cost of commercial ceramic membranes, estimated to be in the range of USD 500–1000 m^{-2} [9]. The cost of the membrane active layer was estimated to be USD 8.13 m^{-2}, bringing the membrane cost to roughly USD 14.3 m^{-2}.

Table 6. Cost estimation of the optimized UF membrane.

		Item	**Unit price**	**Cost estimation (USD m^{-2})**
Pyrophyllite support	Materials	Pyrophyllite	0.08 USD kg^{-1}	0.906
	Energy	Grinder (1250 W)	0.118 USD kWh^{-1}	0.0278
		Sifter (125 W)	0.118 USD kWh^{-1}	0.0044
		Furnace (3000 W)	0.118 USD kWh^{-1}	5.20
	Total cost		USD **6.14 m^{-2}**	
Membrane active layer	Materials	Pyrophyllite	0.08 USD kg^{-1}	0.0136
		PVA	21.90 USD kg^{-1}	3.72
		HCl	32 USD kg^{-1}	0.110
	Energy	Furnace (3000 W)	0.118 USD kWh^{-1}	4.28
		Stirring (550 W)	0.118 USD kWh^{-1}	0.0137
	Total cost		USD **8.13m^{-2}**	

Total cost of membrane	USD **14.3 m^{-2}**

4. Conclusion

This study indicates the effectiveness of ceramic membrane based on purified pyrophyllite as an efficient and potentially cost-effective solution for wastewater treatment. Suitable pyrophyllite purification improved membrane performance by enhancing surface uniformity and removing impurities, enhancing membrane selectivity in terms of dye rejection. The microstructure of the membrane was also affected by the sintering temperature, which had a major impact on performance. Increasing the temperature from 1000 to 1050 °C improved dye rejection while slightly reducing flux, due to active layer densification. Balance between permeability and selectivity was achieved at 1050 °C. The most promising SC1050 membrane exhibited excellent water permeability (86 L m^{-2} h^{-1} bar^{-1}), fouling behavior, and a rejection rate exceeding 92% for different dyes with molecular weight between roughly 300 and 1400 g mol^{-1}, underscoring its suitability for industrial applications. The economic viability of this membrane, with an estimated fabrication cost of USD 14.3 m^{-2}, suggests that this ceramic membrane may be a promising alternative for applications requiring scalable, environmentally-friendly solutions. To strengthen the practical relevance of this work, future studies shall focus on evaluating the mechanical and chemical stability of the membrane, as well as its durability. A promising avenue for future development is also the integration of pyrophyllite-based membranes with advanced fabrication techniques, such as additive manufacturing (e.g., 3D printing). These methods could enable more precise control over membrane geometry, pore architecture, and layer thickness. Further research is warranted to explore the practical aspects of scaling up membrane fabrication and to systematically evaluate the benefits and challenges, both economic and technological, associated with the proposed membrane.

Acknowledgements

The authors express their thanks to the Moroccan institution of "Hassan II Academy of Science and Technology" ID: ELA5580689, for their financial support. Project name: "Multidisciplinary research on geomaterials and the volcanic geosites of Morocco: Need for their valorization and their utilization in the perspective of a sustainable development

References

[1] X. Wang, J. Jiang, W. Gao, Reviewing textile wastewater produced by industries: characteristics, environmental impacts, and treatment strategies, Water Sci. Technol. 85 (2022) 2076–2096. https://doi.org/10.2166/wst.2022.088.

[2] D. El Machtani Idrissi, A. Essate, Y. Kouzi, B. Achiou, D. Beqqour, A. Aaddane, A.-E. Reghai, S. Alami Younssi, M. Ouammou, Green synthesis of ZnO using olives leaf extract: Parameters optimization and its application on adsorption and photocatalytic degradation of direct red 80, Ceram. Int. (2025) S0272884225001737. https://doi.org/10.1016/j.ceramint.2025.01.161.

[3] Z. Chafiq Elidrissi, D. El Machtani Idrissi, Y. Kouzi, B. Achiou, S. Tahiri, M. Ouammou, S. Alami Younssi, Effective conversion of fly ash waste into Na-P1 zeolite and its application on the adsorption of Cr(VI), Inorg. Chem. Commun. 156 (2023) 111192. https://doi.org/10.1016/j.inoche.2023.111192.

[4] A. Essate, D. El Machtani Idrissi, B. Achiou, S. Adlane, M. Breida, S. Curcio, S. Chakraborty, S. Alami Younssi, M. Ouammou, High-performance zeolite-A/polystyrene composite membrane tailored for efficient soluble dyes separation and antifouling, Colloids Surf. Physicochem. Eng. Asp. 703 (2024) 135162. https://doi.org/10.1016/j.colsurfa.2024.135162.

[5] A. Talidi, A. Bouazizi, A. Essate, A. Karim, A. Aaddane, M. Ouammou, R. Saadani, S. Alami Younssi, Manufacture and characterization of flat microfiltration membrane based on Moroccan pyrophyllite clay for pretreatment of raw seawater for desalination,

DESALINATION WATER Treat. 253 (2022) 24–38. https://doi.org/10.5004/dwt.2022.28260.

[6] X. Ke, Y. Huang, T.R. Dargaville, Y. Fan, Z. Cui, H. Zhu, Modified alumina nanofiber membranes for protein separation, Sep. Purif. Technol. 120 (2013) 239–244. https://doi.org/10.1016/j.seppur.2013.10.011.

[7] N. Kageyama, A. Takagaki, T. Sugawara, R. Kikuchi, S.T. Oyama, Synthesis and characterization of a silica-alumina composite membrane and its application in a membrane reactor, Sep. Purif. Technol. 195 (2018) 437–445. https://doi.org/10.1016/j.seppur.2017.12.021.

[8] F. Jiang, H. Li, Z. Di, S. Sui, Q. Yu, J. Zhang, Silica ultrafiltration membrane with tunable pore size for macromolecule separation, J. Membr. Sci. 441 (2013) 25–30. https://doi.org/10.1016/j.memsci.2013.04.008.

[9] F.Z. Charik, B. Achiou, A. Belgada, Z.C. Elidrissi, M. Ouammou, M. Rabiller-Baudry, S.A. Younssi, Optimal preparation of low-cost and high-permeation NaA zeolite membrane for effective ethanol dehydration, Microporous Mesoporous Mater. 344 (2022) 112229. https://doi.org/10.1016/j.micromeso.2022.112229.

[10] D. El Machtani Idrissi, Z.C. Elidrissi, B. Achiou, M. Ouammou, S. Alami Younssi, Fabrication of low-cost kaolinite/perlite membrane for microfiltration of dairy and textile wastewaters, J. Environ. Chem. Eng. 11 (2023) 109281. https://doi.org/10.1016/j.jece.2023.109281.

[11] D. Zou, Y. Fan, State-of-the-art developments in fabricating ceramic membranes with low energy consumption, Ceram. Int. 47 (2021) 14966–14987. https://doi.org/10.1016/j.ceramint.2021.02.195.

[12] P. Belibi Belibi, M.M.G. Nguemtchouin, M. Rivallin, J. Ndi Nsami, J. Sieliechi, S. Cerneaux, M.B. Ngassoum, M. Cretin, Microfiltration ceramic membranes from local

Cameroonian clay applicable to water treatment, Ceram. Int. 41 (2015) 2752–2759. https://doi.org/10.1016/j.ceramint.2014.10.090.

[13] F.Z. Charik, B. Achiou, A. Belgada, M. Ouammou, M. Rabiller-Baudry, S. Alami Younssi, In-depth exploration of defects in zeolite membranes: Typology, formation, characterization and healing, J. Environ. Chem. Eng. 12 (2024) 112918. https://doi.org/10.1016/j.jece.2024.112918.

[14] A. Harrati, Y. Arkame, S. Adlane, A. Essate, B. Achiou, A. El Bouari, A. Aaddane, S. Alami Younssi, C. Sadik, Preparation of low-cost peridotite ceramic microfiltration membrane for treating industrial wastewater, Int. J. Appl. Ceram. Technol. 21 (2024) 4366–4379. https://doi.org/10.1111/ijac.14852.

[15] H. Ouaddari, A. Karim, B. Achiou, S. Saja, A. Aaddane, J. Bennazha, I. El Amrani El Hassani, M. Ouammou, A. Albizane, New low-cost ultrafiltration membrane made from purified natural clays for direct Red 80 dye removal, J. Environ. Chem. Eng. 7 (2019) 103268. https://doi.org/10.1016/j.jece.2019.103268.

[16] A. Boulkrinat, F. Bouzerara, A. Harabi, K. Harrouche, S. Stelitano, F. Russo, F. Galiano, A. Figoli, Synthesis and characterization of ultrafiltration ceramic membranes used in the separation of macromolecular proteins, J. Eur. Ceram. Soc. 40 (2020) 5967–5973. https://doi.org/10.1016/j.jeurceramsoc.2020.06.060.

[17] M. Ben Ali, N. Hamdi, M.A. Rodriguez, K. Mahmoudi, E. Srasra, Preparation and characterization of new ceramic membranes for ultrafiltration, Ceram. Int. 44 (2018) 2328–2335. https://doi.org/10.1016/j.ceramint.2017.10.199.

[18] Y. Jeong, S. Lee, S. Hong, C. Park, Preparation, characterization and application of low-cost pyrophyllite-alumina composite ceramic membranes for treating low-strength domestic wastewater, J. Membr. Sci. 536 (2017) 108–115. https://doi.org/10.1016/j.memsci.2017.04.068.

[19] Y. Jeong, K. Cho, E.E. Kwon, Y.F. Tsang, J. Rinklebe, C. Park, Evaluating the feasibility of pyrophyllite-based ceramic membranes for treating domestic wastewater in anaerobic ceramic membrane bioreactors, Chem. Eng. J. 328 (2017) 567–573. https://doi.org/10.1016/j.cej.2017.07.080.

[20] M. Mohamed Bazin, N. Ahmad, Y. Nakamura, Preparation of porous ceramic membranes from Sayong ball clay, J. Asian Ceram. Soc. 7 (2019) 417–425. https://doi.org/10.1080/21870764.2019.1658339.

[21] T. Ahmad, C. Guria, A. Mandal, Synthesis, characterization and performance studies of mixed-matrix poly(vinyl chloride)-bentonite ultrafiltration membrane for the treatment of saline oily wastewater, Process Saf. Environ. Prot. 116 (2018) 703–717. https://doi.org/10.1016/j.psep.2018.03.033.

[22] R.V. Kumar, A.K. Ghoshal, G. Pugazhenthi, Fabrication of zirconia composite membrane by in-situ hydrothermal technique and its application in separation of methyl orange, Ecotoxicol. Environ. Saf. 121 (2015) 73–79. https://doi.org/10.1016/j.ecoenv.2015.05.006.

[23] Y. Miyah, A. Lahrichi, M. Idrissi, S. Boujraf, H. Taouda, F. Zerrouq, Assessment of adsorption kinetics for removal potential of Crystal Violet dye from aqueous solutions using Moroccan pyrophyllite, J. Assoc. Arab Univ. Basic Appl. Sci. 23 (2017) 20–28. https://doi.org/10.1016/j.jaubas.2016.06.001.

[24] H.A.M. Ahmed, N. Khairy, M.A. Ali, Iron Removal from Low-Grade Pyrophyllite Ore by Microwave Irradiation and Dry Magnetic Separation, Appl. Sci. 14 (2024) 6651. https://doi.org/10.3390/app14156651.

[25] P.G. Bhukte, G.T. Daware, M.J. Chaddha, T.P. Bhosale, A. Agnihotri, Characterization and Beneficiation of Pyrophyllite, in: K. Randive, A.K. Nandi, P.K. Jain, S. Jawadand

(Eds.), Curr. Trends Miner.-Based Prod. Util. Wastes Recent Stud. India, Springer Nature Switzerland, Cham, 2024: pp. 159–167. https://doi.org/10.1007/978-3-031-50262-0_12.

[26] Y. Ettahiri, L. Bouna, J.V. Hanna, A. Benlhachemi, H.L. Pilsworth, A. Bouddouch, B. Bakiz, Pyrophyllite clay-derived porous geopolymers for removal of methylene blue from aqueous solutions, Mater. Chem. Phys. 296 (2023) 127281. https://doi.org/10.1016/j.matchemphys.2022.127281.

[27] H. Wu, M. He, S. Wu, M. Yang, X. Liu, Near-Infrared Spectroscopy Study of OH Stretching Modes in Pyrophyllite and Talc, Crystals 12 (2022) 1759. https://doi.org/10.3390/cryst12121759.

[28] G. Li, J. Zeng, J. Luo, M. Liu, T. Jiang, G. Qiu, Thermal transformation of pyrophyllite and alkali dissolution behavior of silicon, Appl. Clay Sci. 99 (2014) 282–288. https://doi.org/10.1016/j.clay.2014.07.011.

[29] C. Xu, Y. Feng, H. Li, Y. Li, Y. Yao, Purification of natural palygorskite clay: Process optimization, cleaner production, mineral characterization, and decolorization performance, Appl. Clay Sci. 250 (2024) 107268. https://doi.org/10.1016/j.clay.2024.107268.

[30] Y. Kouzi, Z. Chafiq Elidrissi, B. Achiou, D. Beqqour, S. Alami Younssi, M. Rabiller-Baudry, M. Bouhria, M. Ouammou, Enhancing stability and performance of graphene oxide membrane grafted on low-cost rich-silica support: A comparative study of two activation approaches, Process Saf. Environ. Prot. 188 (2024) 1574–1583. https://doi.org/10.1016/j.psep.2024.06.015.

[31] S.L. Sandhya Rani, R.V. Kumar, Insights on applications of low-cost ceramic membranes in wastewater treatment: A mini-review, Case Stud. Chem. Environ. Eng. 4 (2021) 100149. https://doi.org/10.1016/j.cscee.2021.100149.

[32] J. Li, M. Mubashar, R. Zulekha, C. Xu, X. Zhang, Applications of coagulation-sedimentation and ultrafiltration for the removal of nanoparticles from water, Sep. Purif. Technol. 357 (2025) 129920. https://doi.org/10.1016/j.seppur.2024.129920.

[33] R. Shoshaa, M.Y. Ashfaq, M.A. Al-Ghouti, Recent developments in ultrafiltration membrane technology for the removal of potentially toxic elements, and enhanced antifouling performance: A review, Environ. Technol. Innov. 31 (2023) 103162. https://doi.org/10.1016/j.eti.2023.103162.

[34] W. Yan, N. Li, Y. Li, G. Liu, B. Han, J. Xu, Effect of particle size on microstructure and strength of porous spinel ceramics prepared by pore-forming in situ technique, Bull. Mater. Sci. 34 (2011) 1109–1112. https://doi.org/10.1007/s12034-011-0155-8.

[35] M. Zaffar, S.-G. Lu, Pore Size Distribution of Clayey Soils and Its Correlation with Soil Organic Matter, Pedosphere 25 (2015) 240–249. https://doi.org/10.1016/S1002-0160(15)60009-1.

[36] M. Erdemoğlu, Zeta Potential of Pyrophyllite in Aqueous Solutions of Alkaline and Alkaline Earth Metal Cations and Low-Molecular-Weight Organic Anions, J. Dispers. Sci. Technol. 28 (2007) 689–695. https://doi.org/10.1080/01932690701341793.

[37] G. Liang, W. Chen, A.V. Nguyen, T.A.H. Nguyen, Red mud carbonation using carbon dioxide: Effects of carbonate and calcium ions on goethite surface properties and settling, J. Colloid Interface Sci. 517 (2018) 230–238. https://doi.org/10.1016/j.jcis.2018.02.006.

[38] I. Ćurić, D. Dolar, J. Horvat, K. Grgić, Effect of Textile Wastewater Secondary Effluent on UF Membrane Characteristics, Polymers 14 (2022) 2035. https://doi.org/10.3390/polym14102035.

[39] T. Xu, L. Shi, S. Shao, H. Wang, Y. Huang, L. Xing, R. Xia, R. Rossi, L. Zhu, H. Zhu, W. Yang, X. Mao, X. Wang, Dynamic pore modulation of contracted carbon fiber filter for

wastewater treatment: Filtration performance and in-situ regeneration mechanism, Chem. Eng. J. 473 (2023) 145243. https://doi.org/10.1016/j.cej.2023.145243.

[40] H. Liu, X. Song, C. Zhang, Tailor-made highly negatively charged nanofiltration membrane prepared by polyphenol derivatives for anionic dye/salt separation, J. Water Process Eng. 54 (2023) 104068. https://doi.org/10.1016/j.jwpe.2023.104068.

[41] D.O. Obada, D. Dodoo-Arhin, M. Dauda, F.O. Anafi, A.S. Ahmed, O.A. Ajayi, Physico-mechanical and gas permeability characteristics of kaolin based ceramic membranes prepared with a new pore-forming agent, Appl. Clay Sci. 150 (2017) 175–183. https://doi.org/10.1016/j.clay.2017.09.014.

[42] S. Ji, Z. Liu, G. Wang, Y. Liu, Y. Jing, Effects of sintering temperature and particle size on permeability of functionally gradient composite porous materials prepared by hanging slurry process, SN Appl. Sci. 2 (2020) 2046. https://doi.org/10.1007/s42452-020-03794-9.

[43] Q. Hu, M. Wang, Y. Chen, Z. Si, D. Zhang, Effects of sintering temperatures on the microstructure and mechanical properties of S390 powder metallurgy high-speed steel, Front. Mater. 10 (2023) 1198776. https://doi.org/10.3389/fmats.2023.1198776.

[44] J.-H. Eom, H.-J. Yeom, Y.-W. Kim, I.-H. Song, Ceramic Membranes Prepared from a Silicate and Clay-mineral Mixture for Treatment of Oily Wastewater, Clays Clay Miner. 63 (2015) 222–234. https://doi.org/10.1346/CCMN.2015.0630305.

[45] Z. Chafiq Elidrissi, A. Essate, B. Achiou, S. Rode, B. Belaissaoui, S. Alami Younssi, M. Ouammou, High-performance MoS2-based composite membrane for efficient dye/salt separation in textile industry, Sep. Purif. Technol. 376 (2025) 133901. https://doi.org/10.1016/j.seppur.2025.133901.

[46] T. Mahmood, M.T. Saddique, A. Naeem, P. Westerhoff, S. Mustafa, A. Alum, Comparison of Different Methods for the Point of Zero Charge Determination of NiO, Ind. Eng. Chem. Res. 50 (2011) 10017–10023. https://doi.org/10.1021/ie200271d.

[47] A. Essate, B. Achiou, S. Benkhaya, S. Chakraborty, M. Ouammou, S. Alami Younssi, Low-cost polysulfone/polystyrene ultrafiltration membrane with efficient azoic dyes removal and excellent antifouling performance for colored wastewater, Polym. Adv. Technol. 34 (2023) 1279–1292. https://doi.org/10.1002/pat.5969.

[48] Q. Wang, F. Dai, S. Zhang, Z. Ke, C. Chen, G. Qian, Y. Yu, Fabrication of high performance carboxylated poly (aryl ether nitrile) membrane for dye/salt selective separation, Colloids Surf. Physicochem. Eng. Asp. 648 (2022) 129286. https://doi.org/10.1016/j.colsurfa.2022.129286.

[49] R. Ahmad, M. Aslam, G. Jing, D. Kwon, J. Kim, Comparison of pyrophyllite- and alumina-coated membrane treating industrial wastewater in aspect of membrane fouling and organic removal, Process Saf. Environ. Prot. 168 (2022) 1058–1066. https://doi.org/10.1016/j.psep.2022.10.057.

[50] H. Elomari, B. Achiou, D. Beqqour, K. Khaless, R. Beniazza, M. Ouammou, A. Aaddane, S. Alami Younssi, R. Benhida, Preparation and characterization of low-cost zirconia/clay membrane for removal of acid orange 74 dye, Mater. Today Proc. 51 (2022) 1948–1956. https://doi.org/10.1016/j.matpr.2021.03.674.

[51] B. Achiou, S. Adlane, A. Harrati, A. Belgada, A. Aaddane, Z. Chafiq Elidrissi, M. Ouammou, C. Sadik, S. Alami Younssi, Low-cost ceramic peridotite membrane developed with geomaterial-based sintering aids for textile wastewater treatment, J. Environ. Chem. Eng. 13 (2025) 116375. https://doi.org/10.1016/j.jece.2025.116375.

Declaration of interests

☑The authors declare that they have no known competing financial interests or personal relationships that could have appeared to influence the work reported in this paper.

☐ The authors declare the following financial interests/personal relationships which may be considered as potential competing interests:

None.

Graphical abstract

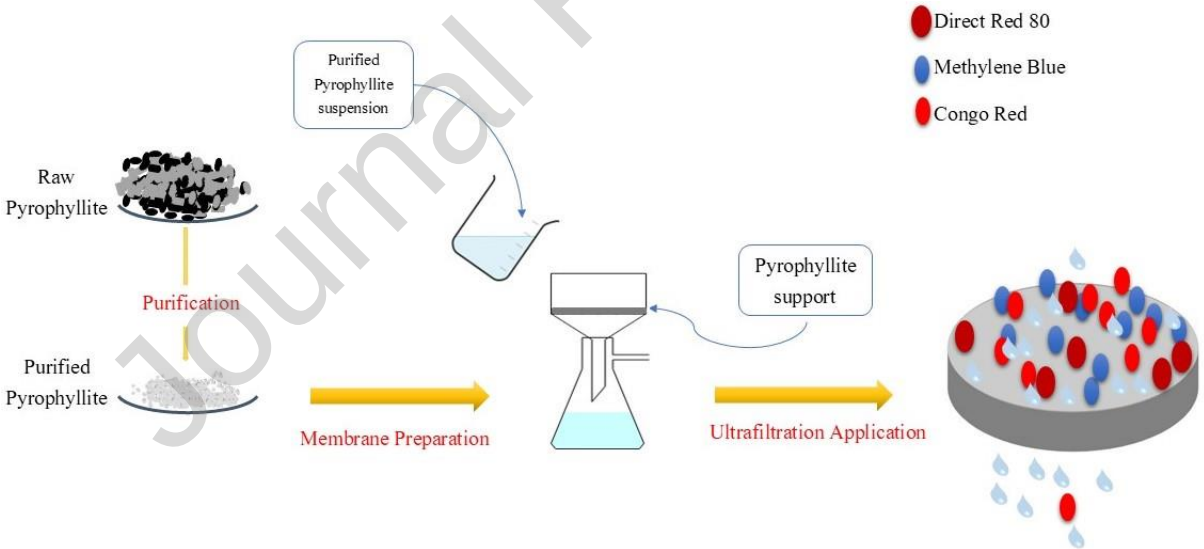

Highlights

- A low-cost purified pyrophyllite ultrafiltration membrane was fabricated.
- The influence of purification level on membrane features was investigated.
- Membrane permeability reached 86 L m^{-2} h^{-1} bar^{-1} with 91.4% DR80 dye rejection.
- The cost of pyrophyllite-based membrane was estimated at USD 14.3 m^{-2}.